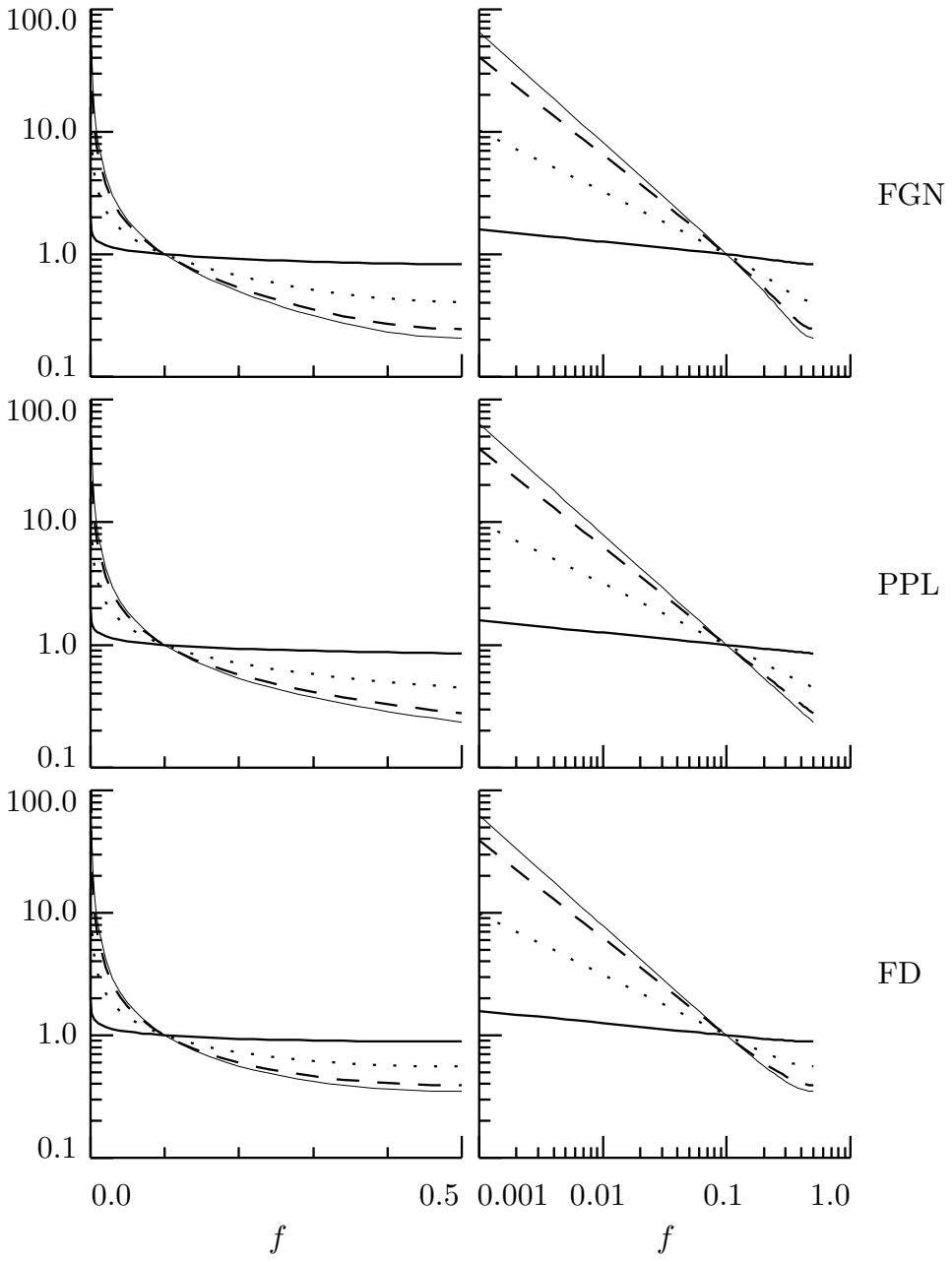

Figure 1. SDFs for FGN, PPL and FD processes (top to bottom rows, respectively) on both linear/log and log/log axes (left- and right-hand columns, respectively). Each SDF $S_X(\cdot)$ is normalized such that $S_X(0.1) = 1$. The table below gives the parameter values for the various plotted curves. (Adapted from Figure 282, Percival and Walden, 2000, copyright Cambridge University Press.)

process	thick solid	dotted	dashed	thin solid
FGN	$H = 0.55$	$H = 0.75$	$H = 0.90$	$H = 0.95$
PPL	$\alpha = -0.1$	$\alpha = -0.5$	$\alpha = -0.8$	$\alpha = -0.9$
FD	$\delta = 0.05$	$\delta = 0.25$	$\delta = 0.40$	$\delta = 0.45$

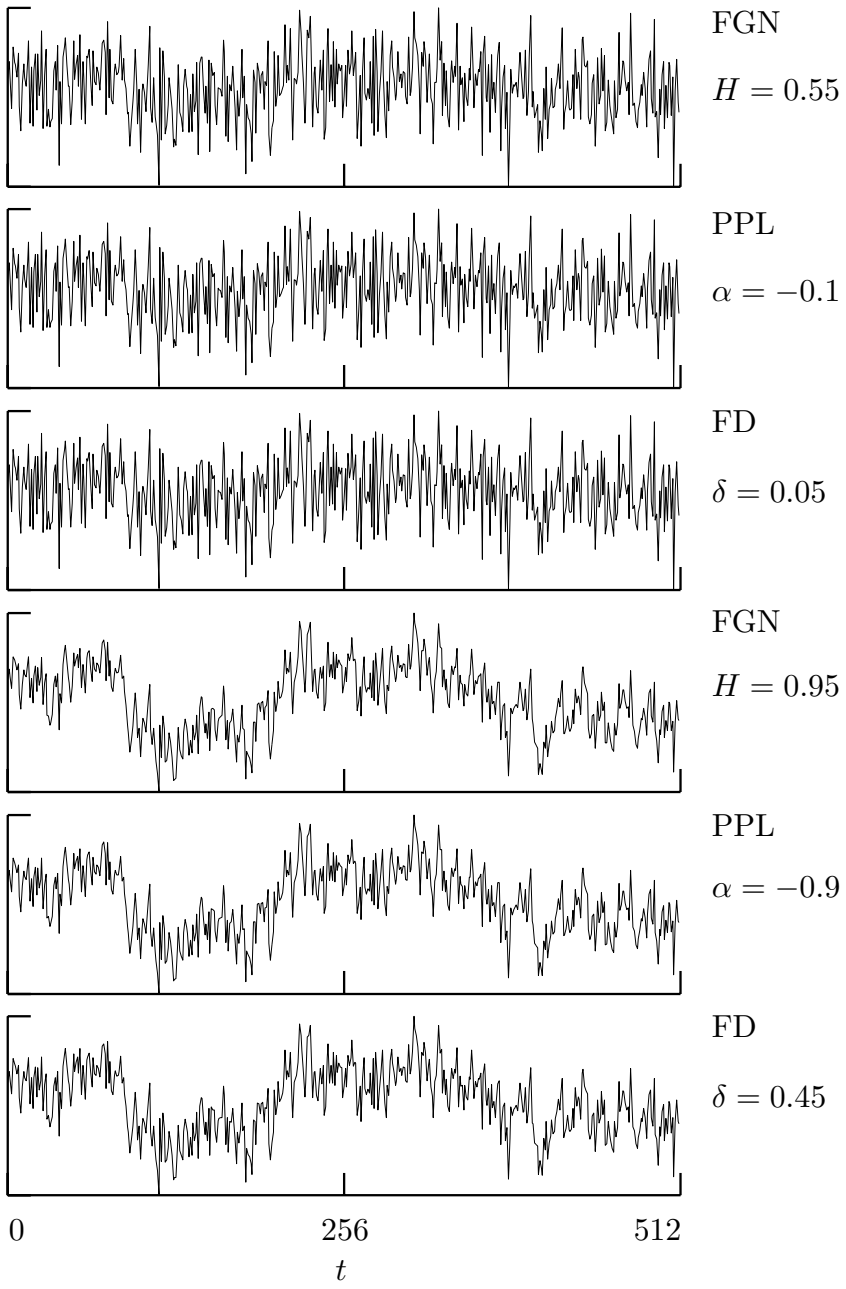

Figure 2. Simulated realizations of FGN, PPL and FD processes. The thick (thin) solid curves in Figure 1 show the SDFs for the top (bottom) three series – these SDFs differ markedly only at high frequencies. We formed each simulated $X_0, \ldots, X_{511}$ using the circulant embedding method, which does so by transforming a realization of a portion $\varepsilon_0, \ldots, \varepsilon_{1023}$ of a white noise process. To illustrate the similarity of FGN, PPL and FD processes with comparable H, α and δ, we used the same ε_t to create all six series. Although the top (bottom) three series appear to be identical, estimates of their SDFs show high frequency differences consistent with their theoretical SDFs. (Adapted from Figure 283, Percival and Walden, 2000, copyright Cambridge University Press.)

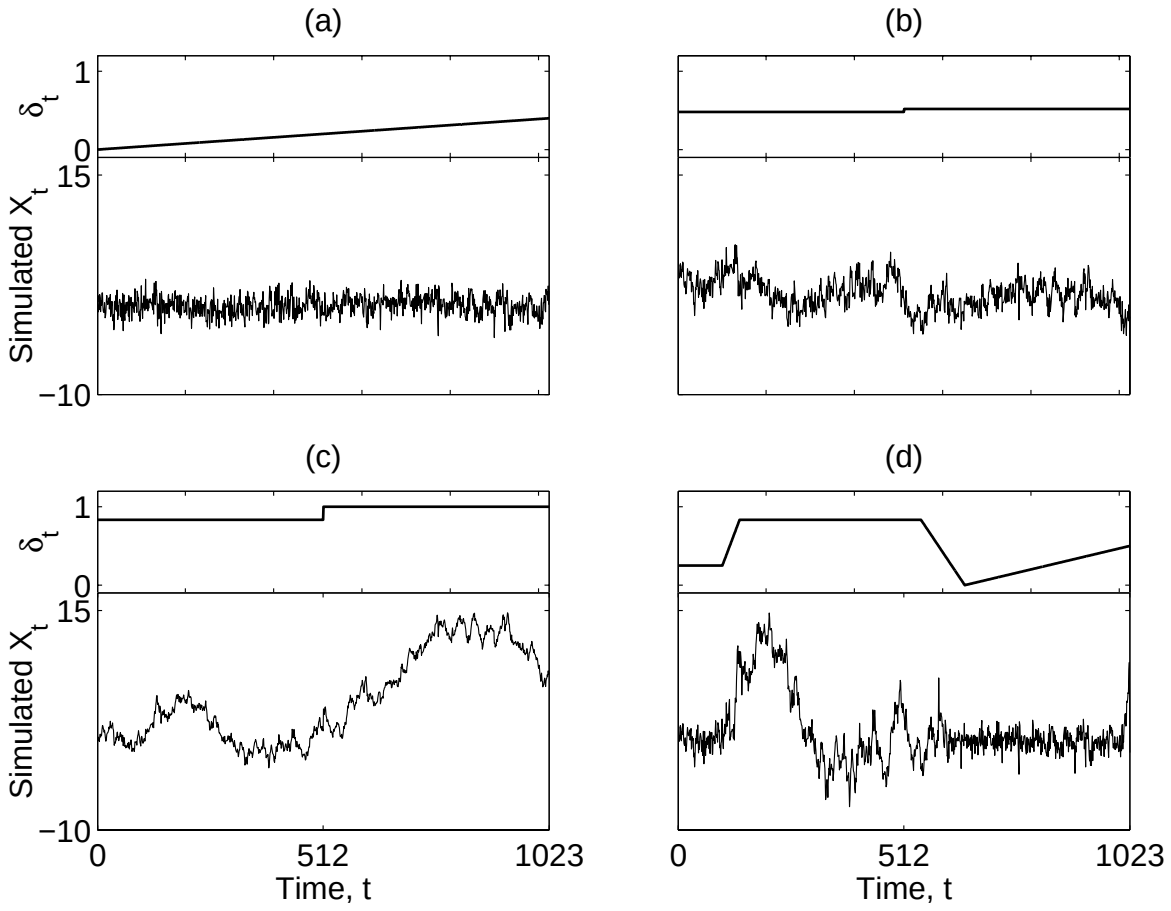

Figure 3. Four examples of time series simulated from TVFD processes. The upper panel of each plot shows the sequence δ_t, $t = 0, \ldots, 1023$, used to generate the simulated time series in the lower panel. All four simulated series were created using the circulant embedding method on the same set of 2048 independent deviates from a standard Gaussian distribution. (Figure 1, Percival and Constantine, 2002.)

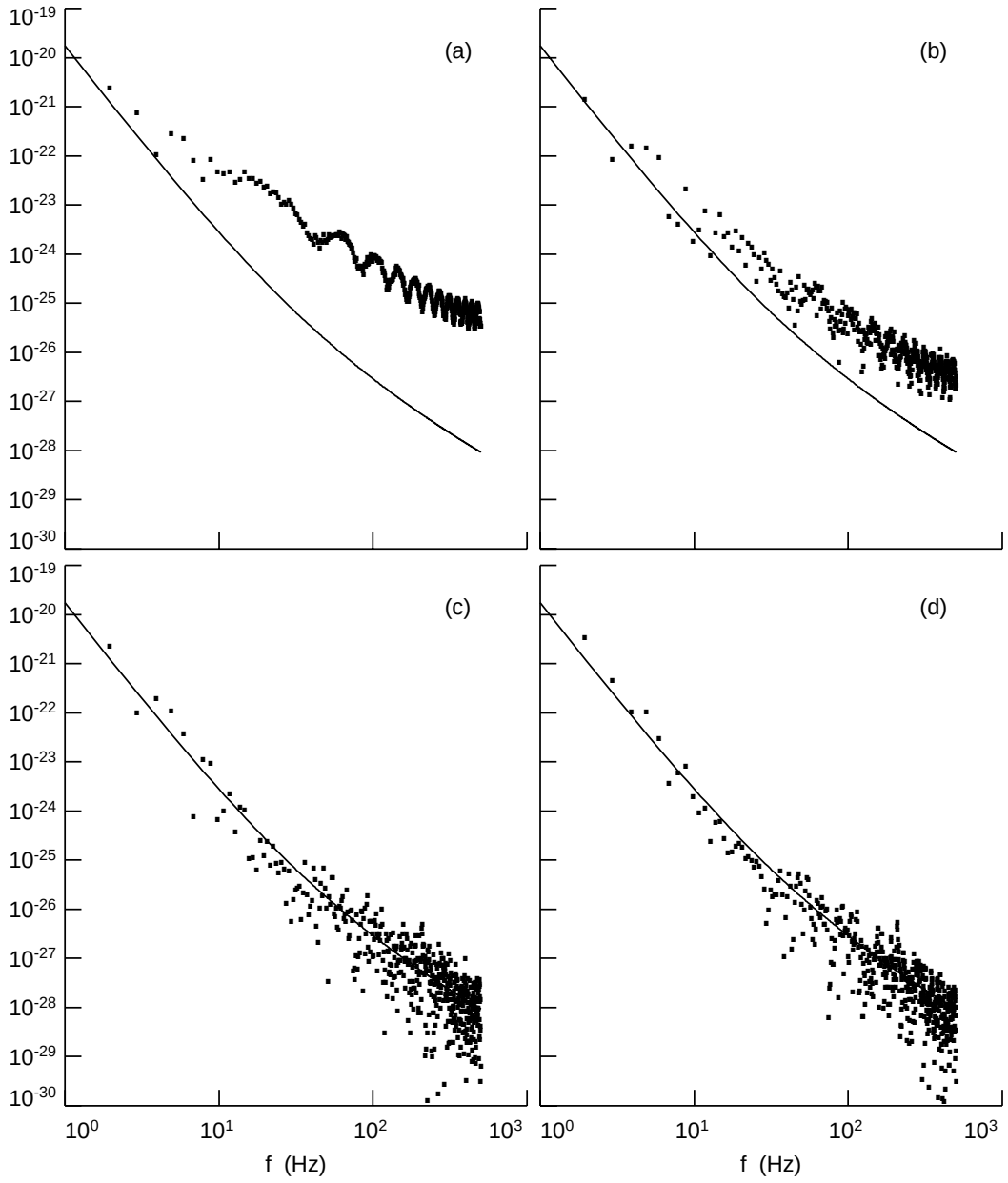

Figure 4. Periodogram (a) and direct spectral estimates (b,c,d) of noise simulated from composite FD process with four components, namely, $\delta = 2, 1.5, 1$ and 0.5 (corresponding to $\alpha = -4, -3, -2$ and -1). The true SDF is the solid curve in each plot, while the dots are the spectral estimates. The data tapers used in the direct spectral estimates are Slepian tapers (i.e., discrete prolate spheroidal sequences) with the resolution bandwidth W set via (b) $NW = 1$, (c) $NW = 2$ and (d) $NW = 4$. The simulated series has length $N = 1000$.

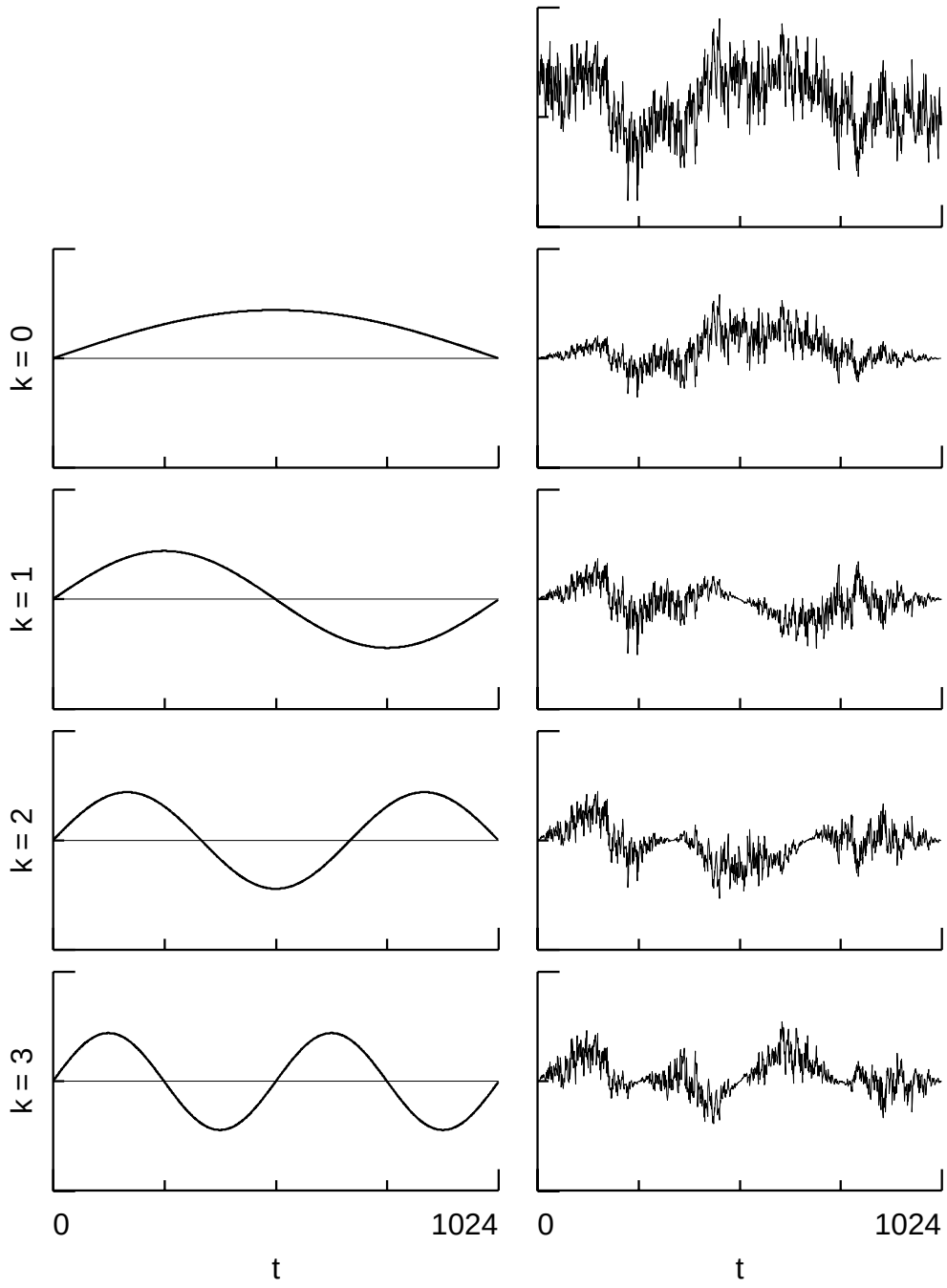

Figure 5. Sinusoidal tapers (left-hand column) as applied to a simulated FD time series with $\delta = 0.45$ (top plot, right-hand column), resulting in tapered series (right-hand column, second to bottom rows).

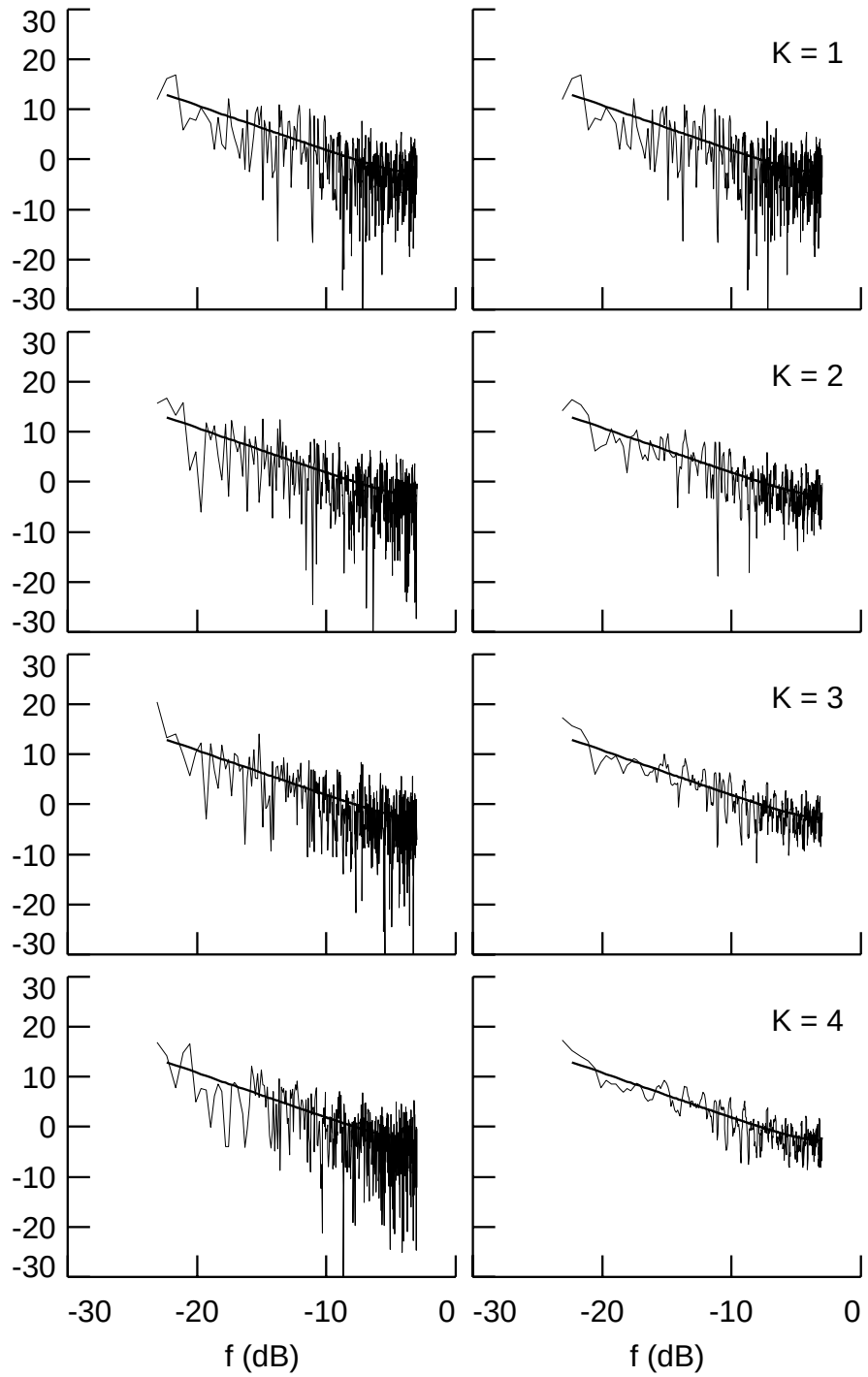

Figure 6. Direct spectral estimates formed using the kth sinusoidal taper, $k = 0, \ldots, 3$ (left-hand column, top to bottom row), along with multitaper estimates formed by averaging $K = 1, \ldots, 4$ of these direct spectral estimates (right-hand column, top to bottom row).

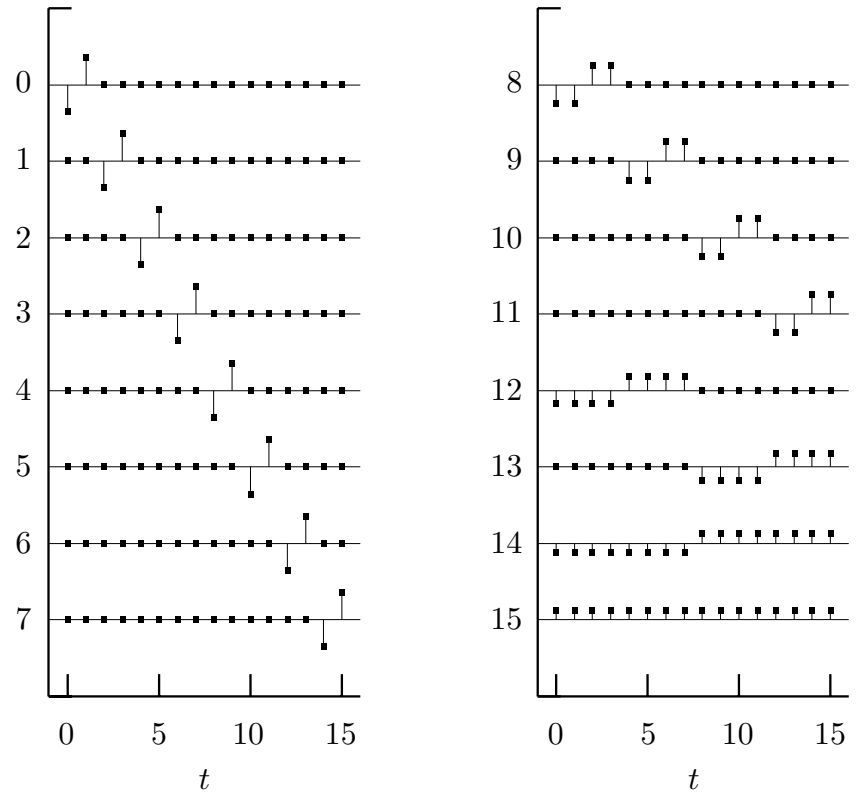

Figure 7. Row vectors $\mathcal{W}_{n\bullet}^T$ of the discrete wavelet transform matrix $\mathcal{W}$ based on the Haar wavelet for $N = 16$ and $n = 0$ to 7 (top to bottom on left plot) and $n = 8$ to 15 (right plot).

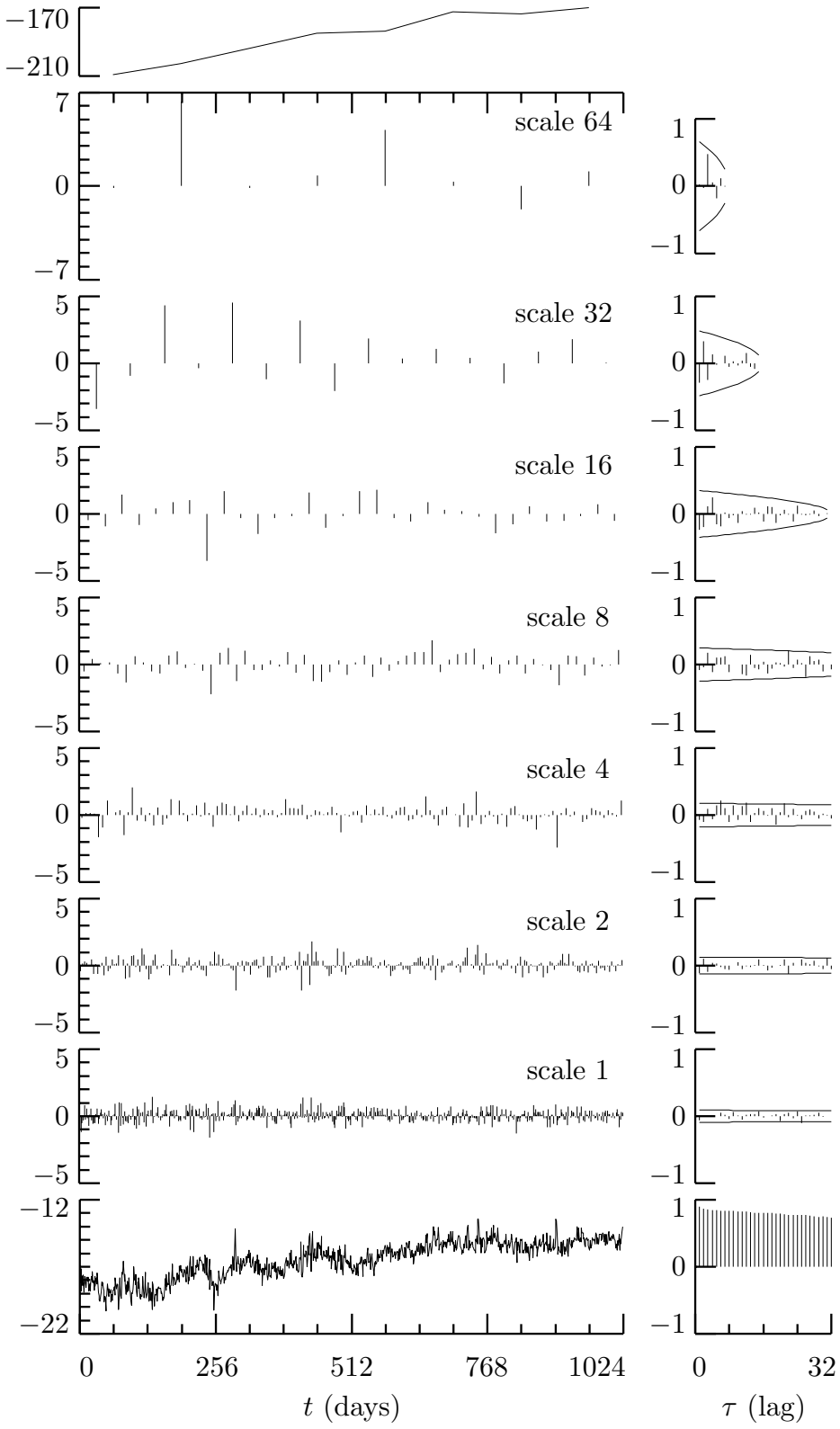

Figure 8. Haar DWT coefficients for clock 571 and sample autocorrelation sequences (ACSs).

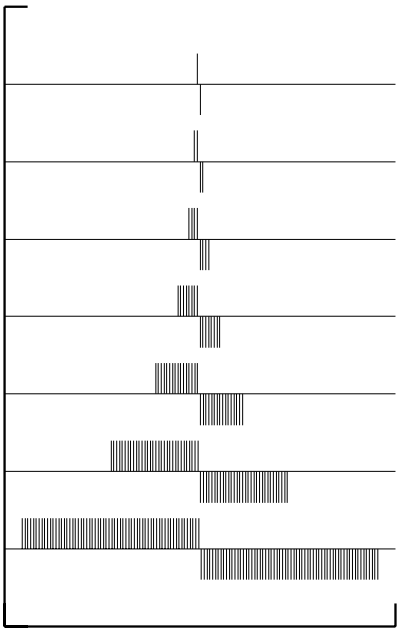

Figure 9. Haar wavelet filters for scales $\tau_j = 2^{j-1}$, $j = 1, 2, \ldots, 7$.

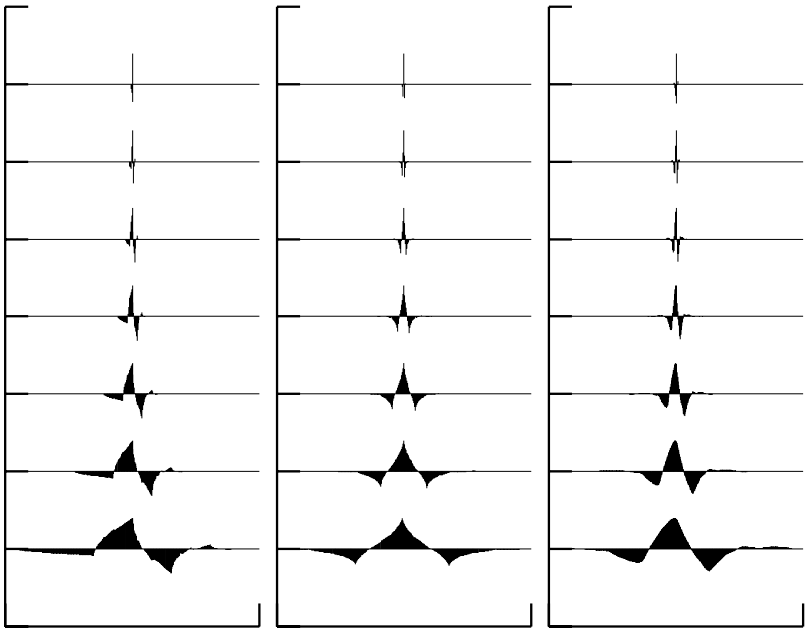

Figure 10. D(4), C(6) and LA(8) wavelet filters for scales $\tau_j = 2^{j-1}$, $j = 1, 2, \ldots, 7$.

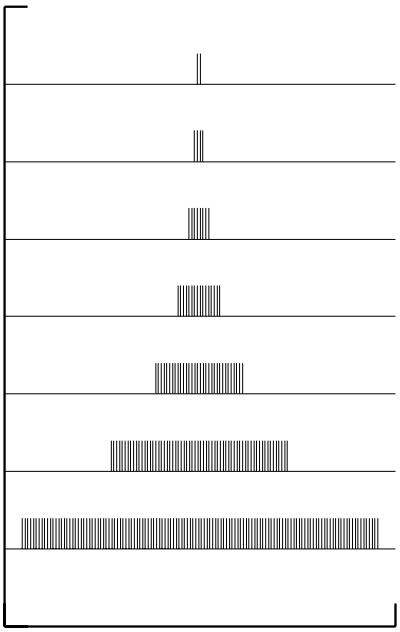

Figure 11. Haar scaling filters for scales $\lambda_{J_0} = 2^{J_0}$, $J_0 = 1, 2, \ldots, 7$.

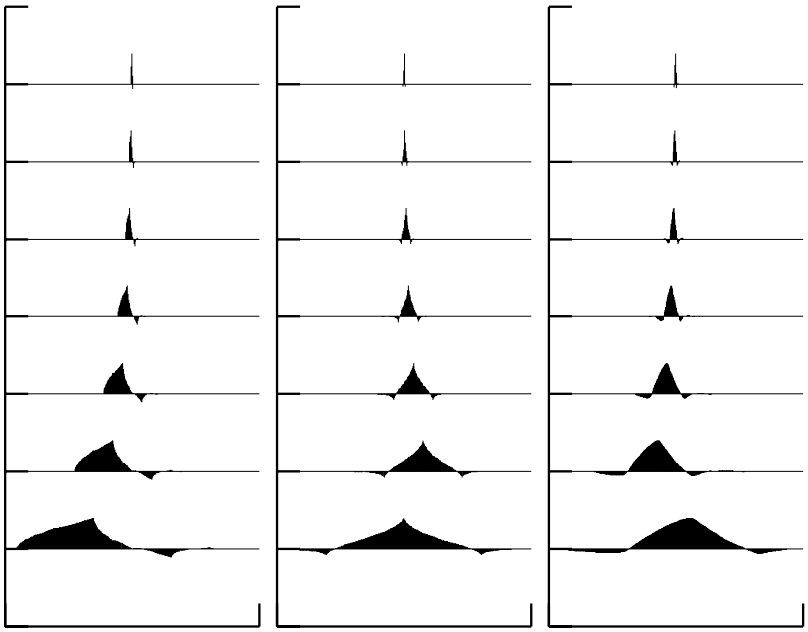

Figure 12. D(4), C(6) and LA(8) scaling filters for scales $\lambda_{J_0} = 2^{J_0}$, $J_0 = 1, 2, \ldots, 7$.

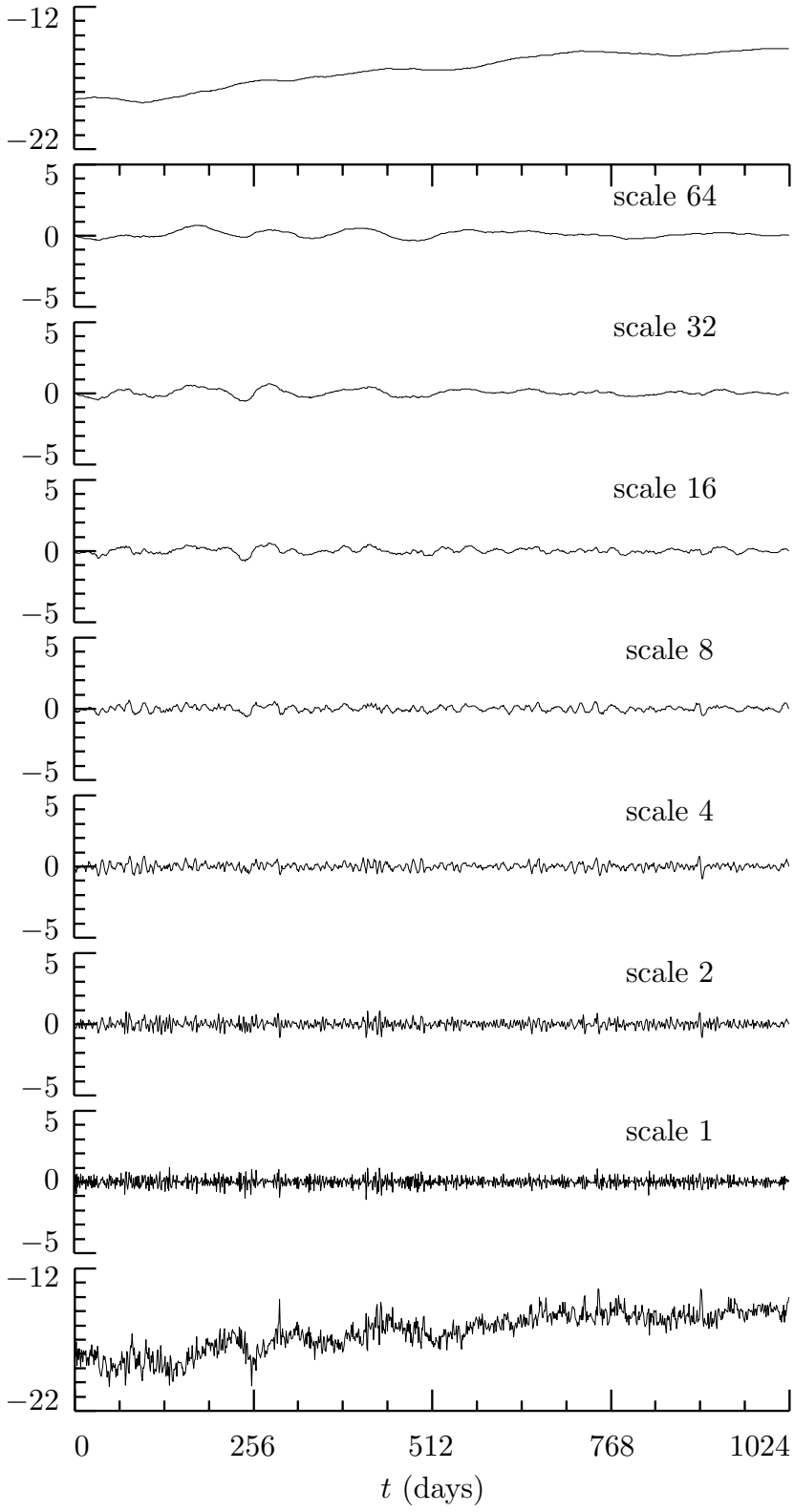

Figure 13. Haar MODWT coefficients for clock 571.

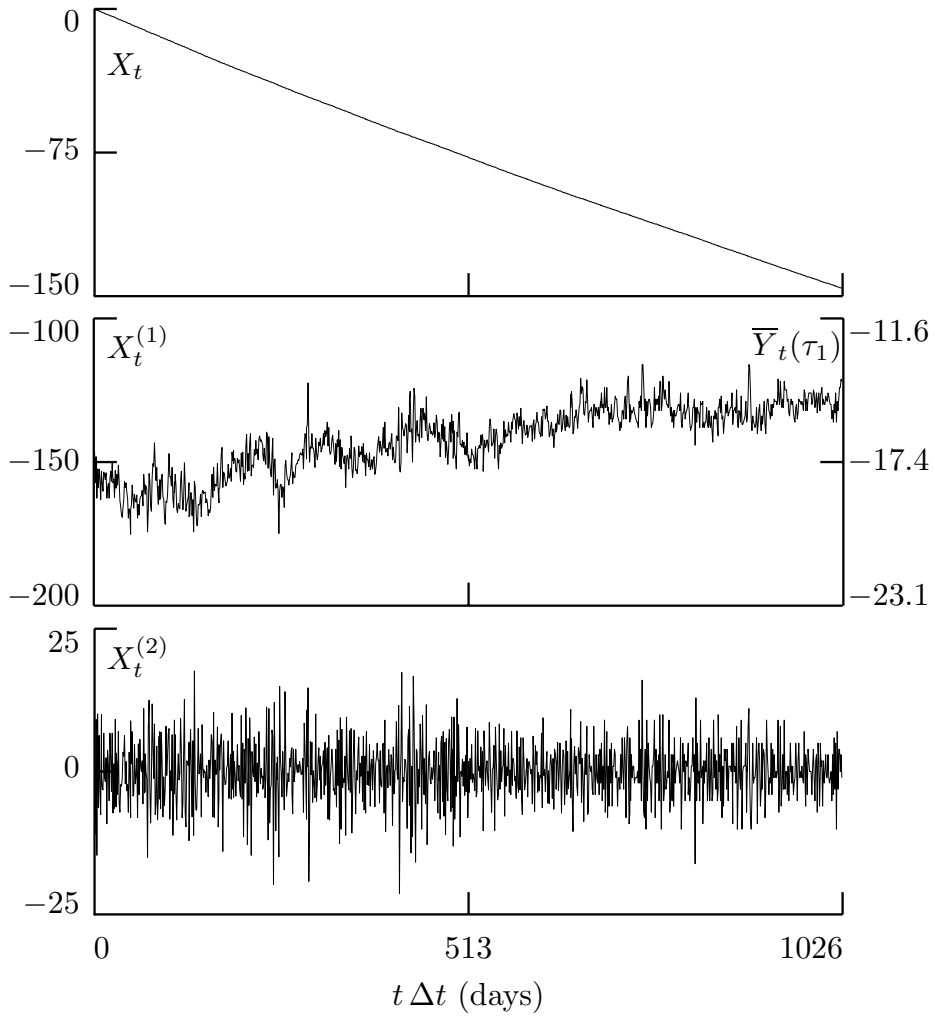

Figure 14. Plot of differences in time $\{X_t\}$ as kept by clock 571 (a cesium beam atomic clock) and as kept by the time scale UTC(USNO) maintained by the US Naval Observatory, Washington, DC (top plot); its first backward difference $\{X_t^{(1)}\}$ (middle); and its second backward difference $\{X_t^{(2)}\}$ (bottom). In the middle plot, $\overline{Y}_t(\tau_1)$ denotes the τ_1 average fractional frequency deviates (given in parts in 10^{13}) – these are proportional to $X_t^{(1)}$.

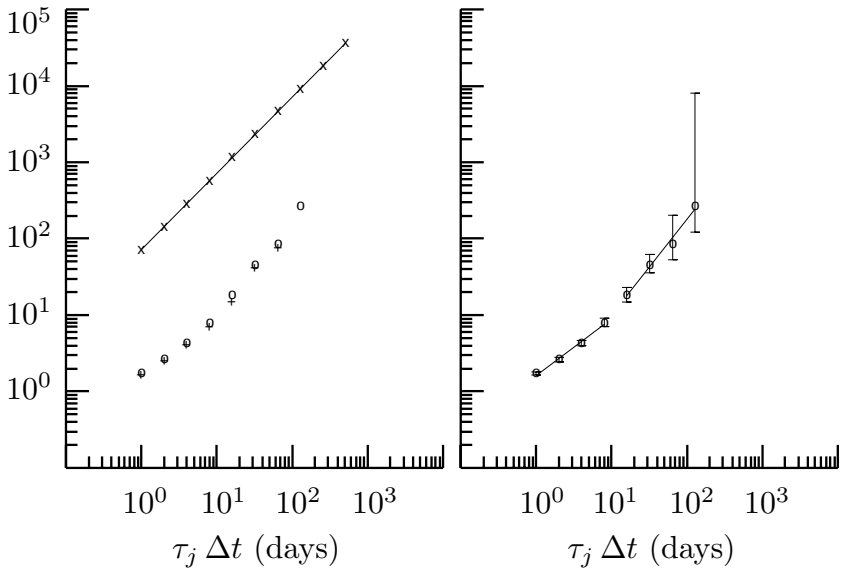

Figure 15. Square roots of wavelet variance estimates for atomic clock time differences $\{X_t\}$ based upon the unbiased MODWT estimator and the following wavelet filters: Haar (x's in left-hand plot, through which a least squares line has been fit), D(4) (circles in left- and right-hand plots) and D(6) (pluses in left-hand plot). The right-hand plot also shows 95% confidence intervals for the unknown wavelet variances.

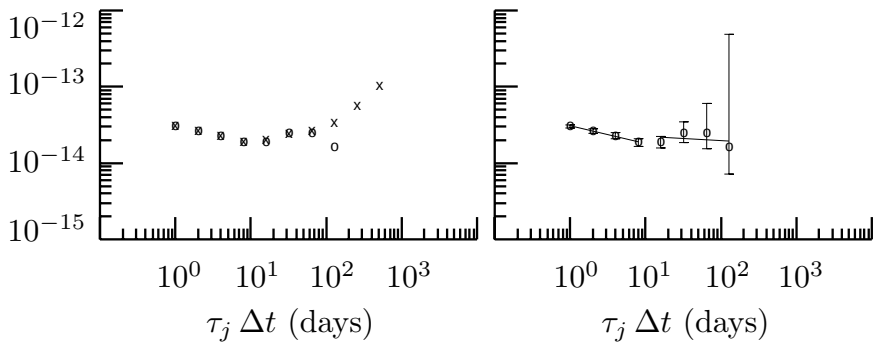

Figure 16. Square roots of wavelet variance estimates for atomic clock one day average fractional frequency deviates $\{\overline{Y}_t(\tau_1)\}$ based upon the unbiased MODWT estimator and the following wavelet filters: Haar (x's in left-hand plot) and D(4) (circles in left and right-hand plots).